Electronic Supplementary Material (ESI) for Physical Chemistry Chemical Physics.

Supplementary Material for: Designing Barrier-Free Metal/MoS$_2$ Contacts through Electrene Insertion

Mohammad Rafiee Diznab,[†] Adrian F. Rumson,[‡] Jesse Maassen,[*,†] and Erin R. Johnson[*,†,‡]

[†]*Department of Physics and Atmospheric Science, Dalhousie University, Halifax, Nova Scotia B3H 4R2, Canada*

[‡]*Department of Chemistry, Dalhousie University, Halifax, Nova Scotia B3H 4R2, Canada*

E-mail: jmaassen@dal.ca; erin.johnson@dal.ca

1 Metal/MoS$_2$ Contacts

To begin, several important features of metal/MoS$_2$ contacts are briefly discussed in order to understand the impact of electrene insertion at this interface. Table S1 summarizes the structural properties and exfoliation energies of the studied metal/MoS$_2$ interfaces. Fig. S1 shows the structures of these interfaces, as well as the computed band structures, MoS$_2$ densities of states, electrostatic potential plots, and Bader charge transfer.

The Schottky barrier height (SBH) for metal/MoS$_2$ contacts can be determined by locating the MoS$_2$ conduction band minimum with respect to the Fermi level of the interface. Despite the hybridization between the metal and MoS$_2$ states (particularly in the case of Cu), the MoS$_2$ band edge can be identified upon comparing the material-projected electronic

Table S 1: Number of atoms, **k**-point mesh, in-plane lattice constant (a), strain on the metal slab (ϵ_m), and interlayer spacing between the metal and the semiconductor ($\bar{d}$) for the Au/MoS_2 and Cu/MoS_2 heterojunctions. Also shown are exfoliation energies computed using either unstrained (unstr) or strained (str) lattice constants for the isolated metal slab, the strain energies, and the decomposition of the strained exfoliation energies into base functional and D3 dispersion contributions. All energies are in meV/Å^2, using the area of the strained unit cell.

Interface	Au/MoS_2	Cu/MoS_2
# atoms	33	105
k-point mesh	$7 \times 7 \times 1$	$4 \times 4 \times 1$
$a\,(= b)$ (Å)	5.46	9.47
ϵ_m (%)	3.26	2.45
$\bar{d}$ (Å)	2.82	2.21
$E_\mathrm{exfo,unstr}$	3.5	59.8
E_strain	48.2	36.7
$E_\mathrm{exfo,str}$	51.7	96.5
$E_\mathrm{base,str}$	-7.8	21.9
$E_\mathrm{disp,str}$	59.5	74.6

bands of the interface with the electronic bands of individual layers (metal and MoS_2) in the same supercell configuration, as depicted in Fig. S2. From the electronic band energies shown in Fig. S1(b,f), the SBHs of Au/MoS_2 and Cu/MoS_2 interfaces are calculated to be $\sim$0.5 eV and 0.4 eV, respectively, in reasonable agreement with literature values.[1–3]

Pristine monolayer MoS_2 physisorbs on Au, as is evident from the dispersion contribution to the exfoliation energy (Table S1), which is slightly higher than the total due to non-bonded repulsion from the base density functional. As such, the top-contacted configuration of the Au/MoS_2 interface shown in Fig. S1(a) has a vdW gap, which causes a tunnelling barrier for electron transport.[4] The electrostatic potential profile of this heterostructure is depicted in Fig. S1(d) and is calculated as the sum of ionic and Hartree contributions, averaged over the xy-plane perpendicular to the interface. The red bar in Fig. S1(d) shows the range of potential values at the point with the highest average potential within the vdW gap. As the minimum of this range lies above the Fermi level, this indicates the presence of a tunnelling barrier. Since the electrostatic potential (relative to the Fermi level) is positive across the whole contact region, no electrons pass through the contact without tunnelling; this is in

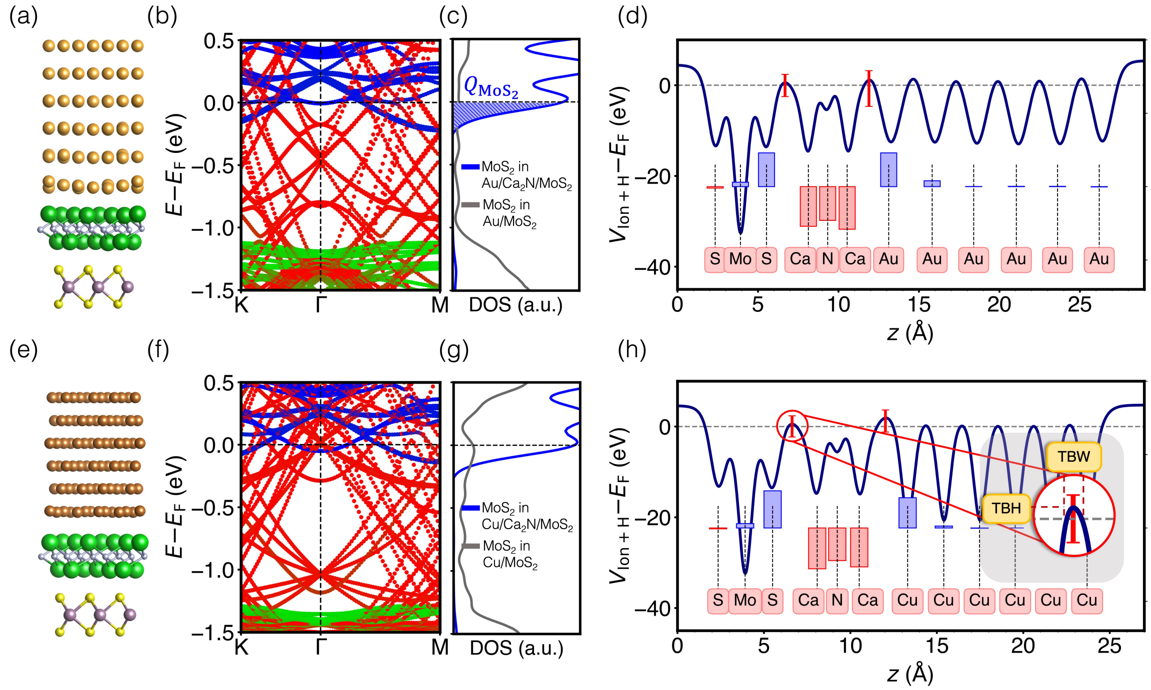

Fig. S1: (a) Optimized geometry, (b) material-projected band structure, (c) densities of MoS_2 states per formula unit, and (d) electrostatic potential for the Au/MoS_2 interface. Panels (e)-(h) present the same quantities for the Cu/MoS_2 interface. In the potential plots, the red bars indicate the range of values at the maximum point within the interface region. The results are overlaid with the differences in Bader atomic charges for the heterostructures, relative to the separated materials. Positive (negative) values indicate accumulation (depletion) of electron density.

addition to the already present Schottky barrier.

Turning to Cu/MoS_2, the range of potential values at the interface extends below the Fermi level, as shown in Fig. S1(h). Thus, while a Schottky barrier also exists for the Cu/MoS_2 heterostructure, our calculations indicate that electrons can travel through some fraction of the interface without tunnelling. Notably, Helfrecht *et al.*[3] showed chemisorption of TMDCs on Cu. Similar to Ti/MoS_2 interfaces,[5,6] partial covalent bonding characteristics can explain the absence of tunnelling barriers at Cu/MoS_2 contacts. We also predict some chemisorption of MoS_2 on Cu, since Table S1 shows a favourable bonding contribution from the base density functional to the exfoliation energy for the Cu/MoS_2 interface.

Finally, the secondary axes in Fig. S1(d,h) show the Bader charge transfer due to interface formation. For the Au/MoS_2 heterostructure in Fig. S1(d), there is effectively zero charge

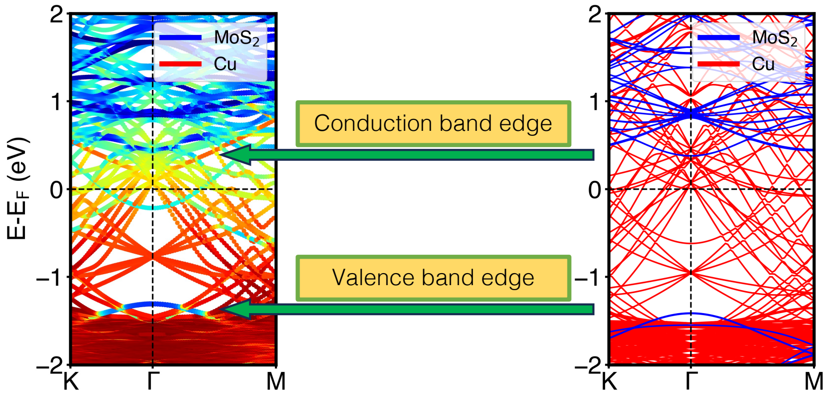

Fig. S 2: Determination of the MoS_2 conduction band edge and SBH for the Cu/MoS_2 interface. Left: The electronic band structure of the Cu/MoS_2 interface; the colour scale indicates the contributions from the Cu slab (red) and MoS_2 (blue). Right: Overlaid electronic band structures of the isolated Cu slab (red) and MoS_2 monolayer (blue) using the same (distorted) geometries as for the full Cu/MoS_2 interface.

transfer, as expected for a vdW contact. Conversely, for the Cu/MoS_2 heterostructure in Fig. S1(f), the negative (red) bar for the Cu atoms nearest the interface indicates depletion of charge from the metal, while the positive (blue) bars illustrate the accumulated charge within the MoS_2. This charge transfer is also an indicator of chemisorption for the Cu/MoS_2 interface.

2 Hybrid Functional Tests on Ca_2N/MoS_2 Contacts

To investigate the effect of delocalization error on our results, calculations were performed for the Ca_2N/MoS_2 interface, using the same interface structure as in Ref. 7. The atomic positions were then optimized using the PBE and HSE06 functionals and the XDM dispersion correction[8] as implemented in the FHI-aims program.[9] The calculations additionally used 'tier1' or 'light' basis sets, 'tier2' or 'tight' integration grids, the ZORA scalar relativity correction,[10] and a $9 \times 9 \times 1$ **k**-point mesh. Figure S3 shows the band structures obtained with both functionals at the corresponding optimized geometries. The two band structures are quite similar overall, although the gap between the Ca_2N nitrogen states and surfaces states is larger with HSE06, as expected. The MoS_2 conduction band also reaches farther below the Fermi level with HSE06, indicating greater charge transfer from Ca_2N to MoS_2.

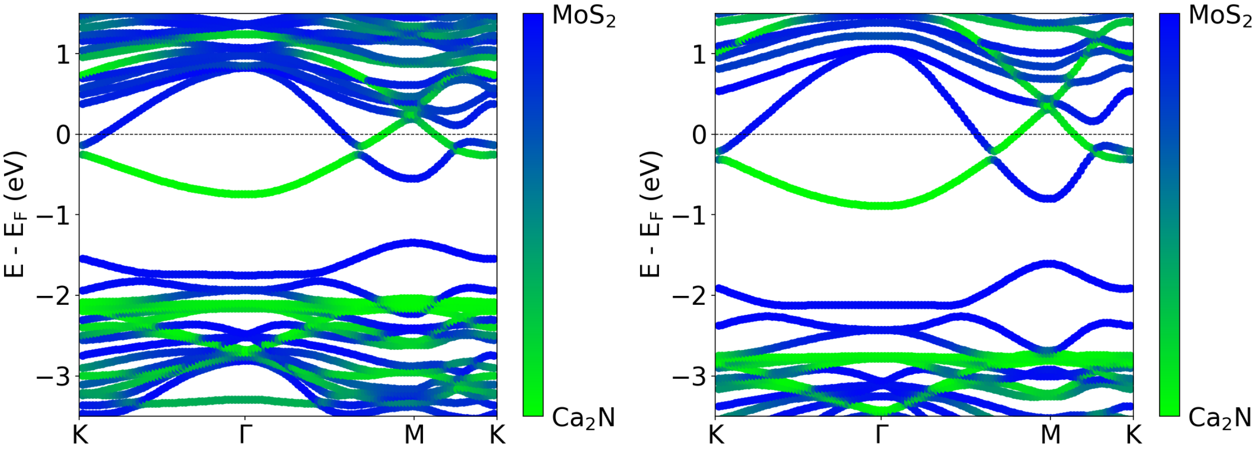

Fig. S 3: Computed materials-projected band structures for the Ca_2N/MoS_2 interface, obtained with the PBE (left) and HSE06 (right) density functionals using the FHI-aims program.

3 Metal/Electrene/MoS$_2$ Contacts

3.1 Construction of Interfaces

Table S 2: Number of atoms, **k**-point mesh, in-plane lattice constants (a), strain on the electrene (ϵ_{e}), strain on the metal slab (ϵ_{Au}), the interlayer distance between the MoS$_2$ and electrene layer ($\bar{d}_{\mathrm{MoS_2}}$) and the interlayer distance between the electrene and metal slab ($\bar{d}_{\mathrm{metal}}$) for the metal/electrene/MoS$_2$ interfaces.

Au/electrene/MoS$_2$

Electrene	Ca$_2$N	Sr$_2$N	Sr$_2$P	Ba$_2$N	Ba$_2$P	Ba$_2$As	Ba$_2$Sb
# atoms	120	162	156	243	234	111	111
k-point mesh	$4 \times 4 \times 1$	$3 \times 3 \times 1$	$3 \times 3 \times 1$	$3 \times 3 \times 1$	$3 \times 3 \times 1$	$4 \times 4 \times 1$	$4 \times 4 \times 1$
$a\,(= b)$ (Å)	9.47	13.75	11.38	13.75	11.38	9.47	9.47
ϵ_{e} (%)	0.16	0.34	2.34	0.39	0.28	1.05	4.28
ϵ_{Au} (%)	3.26	2.57	0.79	2.57	2.57	3.26	3.26
$\bar{d}_{\mathrm{MoS_2}}$ (Å)	2.59	2.70	2.71	2.94	2.86	2.93	2.83
$\bar{d}_{\mathrm{Au}}$ (Å)	2.68	2.85	2.83	2.95	2.92	2.81	2.81

Cu/electrene/MoS$_2$

Electrene	Ca$_2$N	Sr$_2$N	Sr$_2$P	Ba$_2$N	Ba$_2$P	Ba$_2$As	Ba$_2$Sb
# atoms	126	180	174	261	117	117	219
k-point mesh	$4 \times 4 \times 1$	$3 \times 3 \times 1$	$3 \times 3 \times 1$	$3 \times 3 \times 1$	$4 \times 4 \times 1$	$4 \times 4 \times 1$	$3 \times 3 \times 1$
$a\,(= b)$ (Å)	9.47	11.38	11.38	13.75	9.47	9.47	12.62
ϵ_{e} (%)	0.16	0.93	2.34	0.39	3.41	1.05	3.46
ϵ_{Cu} (%)	2.46	1.87	1.87	1.46	2.45	2.45	1.45
$\bar{d}_{\mathrm{MoS_2}}$ (Å)	2.57	2.68	2.65	2.90	2.88	2.88	2.83
$\bar{d}_{\mathrm{Cu}}$ (Å)	2.78	2.85	2.82	2.99	2.93	2.95	2.97

3.2 Strain Energies

Table S 3: Percent strains on the metal slab ($\epsilon_{\mathrm{Au/Cu}}$) and the electrene layer (ϵ_{e}) in metal/electrene/MoS$_2$ heterostructures, along with the component and total strain energies in meV/Å^2 using the area of the strained unit cell.

Au/electrene/MoS$_2$

Electrene	ϵ_{Au} (%)	ϵ_{e} (%)	$E_{\mathrm{strain,Au}}$	$E_{\mathrm{strain,e}}$	E_{strain}
Ca_2N	3.26	0.16	49.1	0.6	49.7
Sr_2N	2.57	0.34	46.4	1.3	47.7
Sr_2P	0.79	2.34	1.6	1.4	3.0
Ba_2N	2.57	0.39	46.5	0.1	46.6
Ba_2P	2.57	2.28	46.6	0.1	46.7
Ba_2As	3.26	1.05	49.3	0.2	49.5
Ba_2Sb	3.26	4.28	49.7	2.8	52.5

Cu/electrene/MoS$_2$

Electrene	ϵ_{Cu} (%)	ϵ_{e} (%)	$E_{\mathrm{strain,Cu}}$	$E_{\mathrm{strain,e}}$	E_{strain}
Ca_2N	2.45	0.16	16.4	0.6	17.0
Sr_2N	1.87	0.93	8.1	0.7	8.8
Sr_2P	1.87	2.34	22.1	1.4	23.5
Ba_2N	1.46	0.39	16.2	0.1	16.3
Ba_2P	2.45	3.40	33.7	2.1	35.8
Ba_2As	2.45	1.05	33.7	0.2	33.9
Ba_2Sb	1.42	3.46	5.8	1.7	7.5

3.3 Bader Charge Transfer

Table S 4: Bader charge transfer values of metal/electrene/MoS_2 interfaces. $Q^{\text{Bader}}_{\text{Electrene}}$ values are the amount of charge transferred from the electrene layer, while $Q^{\text{Bader}}_{\text{MoS}_2}$ and $Q^{\text{Bader}}_{\text{Au/Cu}}$ are charges received by the semiconductor and the metal slabs, respectively. The values are reported in units of electrons per formula unit of the material. Note that the charges do not sum to one because there are different numbers of formula units of each material present in the unit cell.

Au/electrene/MoS_2

	$Q^{\text{Bader}}_{\text{MoS}_2}$ (e^-/f.u.)				$Q^{\text{Bader}}_{\text{Electrene}}$ (e^-/f.u.)				$Q^{\text{Bader}}_{\text{Au}}$ (e^-/f.u.)		
	Ca	Sr	Ba		Ca	Sr	Ba		Ca	Sr	Ba
N	0.26	0.25	0.19	N	-0.80	-0.80	-0.75	N	0.05	0.04	0.04
P	–	0.22	0.15	P	–	-0.85	-0.85	P	–	0.04	0.04
As	–	–	0.14	As	–	–	-0.88	As	–	–	0.03
Sb	–	–	0.18	Sb	–	–	-1.00	Sb	–	–	0.04

Cu/electrene/MoS_2

	$Q^{\text{Bader}}_{\text{MoS}_2}$ (e^-/f.u.)				$Q^{\text{Bader}}_{\text{Electrene}}$ (e^-/f.u.)				$Q^{\text{Bader}}_{\text{Cu}}$ (e^-/f.u.)		
	Ca	Sr	Ba		Ca	Sr	Ba		Ca	Sr	Ba
N	0.28	0.26	0.23	N	-0.77	-0.77	-0.76	N	0.04	0.03	0.03
P	–	0.22	0.16	P	–	-0.85	-0.79	P	–	0.03	0.02
As	–	–	0.16	As	–	–	-0.80	As	–	–	0.02
Sb	–	–	0.18	Sb	–	–	-0.88	Sb	–	–	0.02

3.4 MoS_2 Band Gap Variation in Metal/Electrene/MoS_2 Contacts

Table S 5: MoS_2 valence and conduction band edges and band gaps (eV) in metal/MoS_2 and metal/electrene/MoS_2 interfaces. For comparison, the band gap of pristine MoS_2 is calculated to be 1.77 eV and, as this is a semiconductor, the Fermi level is taken to lie in the middle of the gap.

Electrene	Au			Cu		
	Valence	Conduction	Gap	Valence	Conduction	Gap
None	-1.27	0.49	1.76	-1.30	0.41*	1.71*
Ca_2N	-1.75	-0.14	1.61	-1.84	-0.13	1.71
Sr_2N	-1.89	-0.10	1.79	-1.96	-0.13	1.83
Sr_2P	-2.02	-0.16	1.86	-1.83	-0.08	1.75
Ba_2N	-1.93	-0.08	1.85	-1.95	-0.09	1.86
Ba_2P	-1.96	-0.15	1.81	-1.80	-0.09	1.71
Ba_2As	-1.87	-0.08	1.79	-1.81	-0.09	1.72
Ba_2Sb	-1.85	-0.11	1.74	-1.74	-0.08	1.66

*These values are estimates only due to the high degree of state mixing near the conduction band edge.

3.5 Effect of Sliding the MoS_2 Layer

Table S 6: Changes in various properties of the Cu/Ca_2N/MoS_2 interface as a function of differing initial geometries, with the MoS_2 translated in the a, b lattice directions by a particular fraction of these cell lengths before relaxation. Shown are: the relative energy, ΔE; the Fermi energy, E_{Fermi}; the charge transfer to MoS_2, Q_{MoS_2}; the fraction of the contact area that is Ohmic, F_{Ohmic}; the tunneling barrier height, TBH; and tunneling barrier width, TBW.

Sliding Fraction	ΔE (meV/cell)	E_{Fermi} (eV)	Q_{MoS_2} ($10^{14} e^-/\text{cm}^2$)	F_{Ohmic} (%)	TBH (eV)	TBW (Å)
0.0	0.0	4.61	3.00	32.9	0.496	0.46
0.2	20.9	4.62	2.95	30.9	0.546	0.48
0.4	11.4	4.62	2.94	31.5	0.539	0.48
0.6	18.4	4.62	2.92	31.2	0.547	0.48
0.8	21.7	4.62	2.94	30.7	0.554	0.49

3.6 Summary of Interface Properties

Table S 7: Figures of merit computed for various the metal/electrene/MoS_2 contacts: the charge transfer to MoS_2, Q_{MoS_2}; the fraction of the contact area that is Ohmic, F_{Ohmic}; the tunneling barrier height, TBH; and tunneling barrier width, TBW. Results for the metal/MoS_2 interfaces with no electrene are shown for comparison; note that the Q_{MoS_2} for these two cases results from mid-gap states rather than from the MoS_2 conduction band edge.

Interface	Q_{MoS_2} ($10^{14} e^-/cm^2$)	F_{Ohmic} (%)	TBH (eV)	TBW (Å)
Cu/MoS_2	1.92	30.8	0.72	0.40
Cu/Ca_2N/MoS_2	3.09	32.5	0.54	0.47
Cu/Sr_2N/MoS_2	2.98	27.3	0.72	0.55
Cu/Sr_2P/MoS_2	1.91	21.7	1.03	0.68
Cu/Ba_2N/MoS_2	2.32	17.8	1.07	0.71
Cu/Ba_2P/MoS_2	1.49	10.1	1.37	0.88
Cu/Ba_2As/MoS_2	1.57	12.3	1.41	0.89
Cu/Ba_2Sb/MoS_2	1.55	13.8	1.37	0.85
Au/MoS_2	0.77	0.0	3.01	1.08
Au/Ca_2N/MoS_2	2.28	31.7	0.56	0.49
Au/Sr_2N/MoS_2	2.23	26.4	0.70	0.70
Au/Sr_2P/MoS_2	1.74	19.7	1.05	0.74
Au/Ba_2N/MoS_2	1.88	10.1	1.21	0.78
Au/Ba_2P/MoS_2	1.72	8.8	1.54	0.95
Au/Ba_2As/MoS_2	1.44	9.8	1.62	1.00
Au/Ba_2Sb/MoS_2	1.34	13.6	1.38	0.85

3.7 Electronic Properties of Au/Electrene/MoS_2 Contacts

3.7.1 Au/Ca_2N/MoS_2

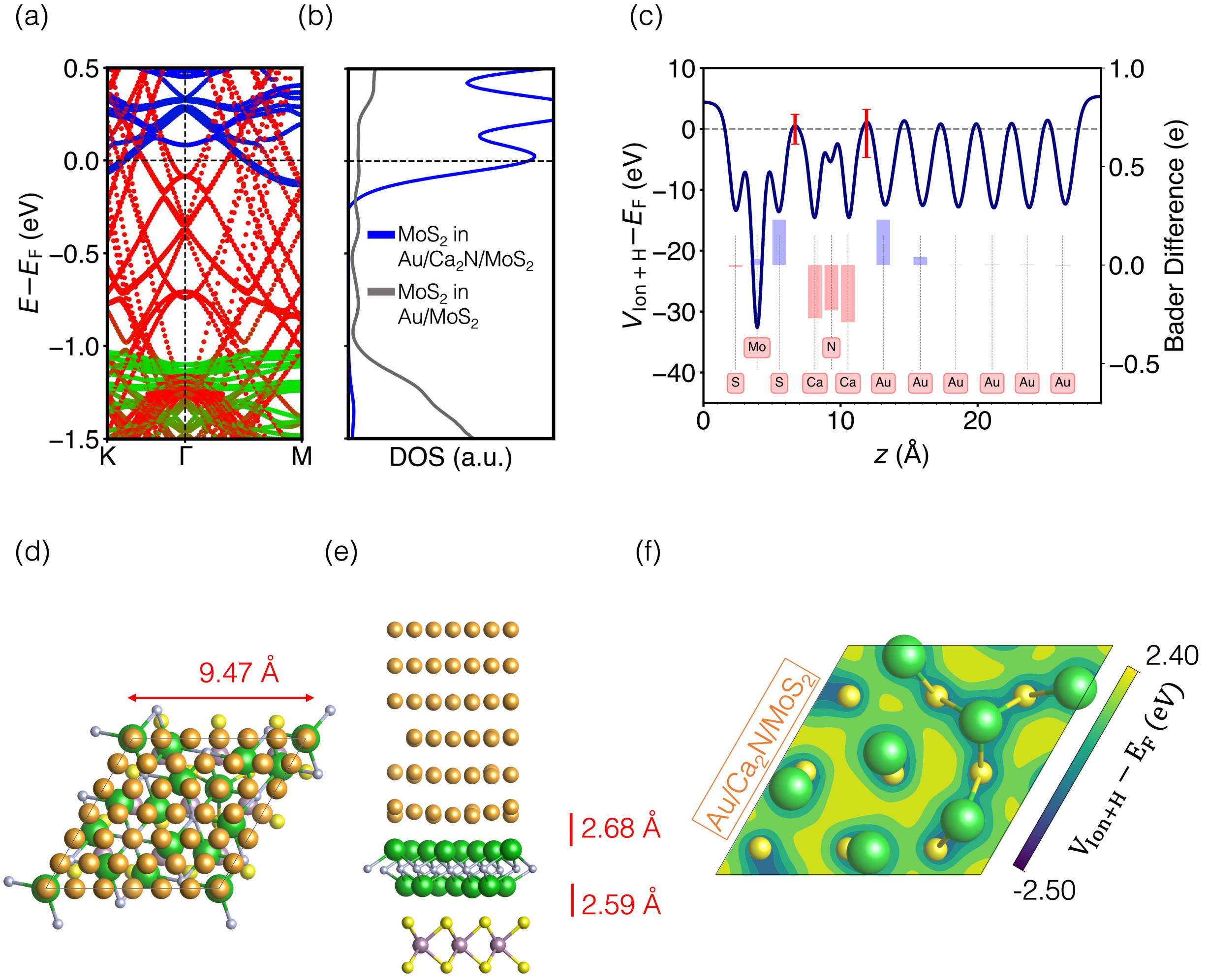

Fig. S4: Properties of the Au/Ca_2N/MoS_2 heterojunction: (a) materials-projected electronic band structure, (b) densities of MoS_2 states per formula unit, (c) averaged electrostatic potential profile, (d) and (e) top and side views of the interface, and (f) 2D projection of the electrostatic potential at the highest potential point of the electrene/MoS_2 interface.

3.7.2 Au/Sr_2N/MoS_2

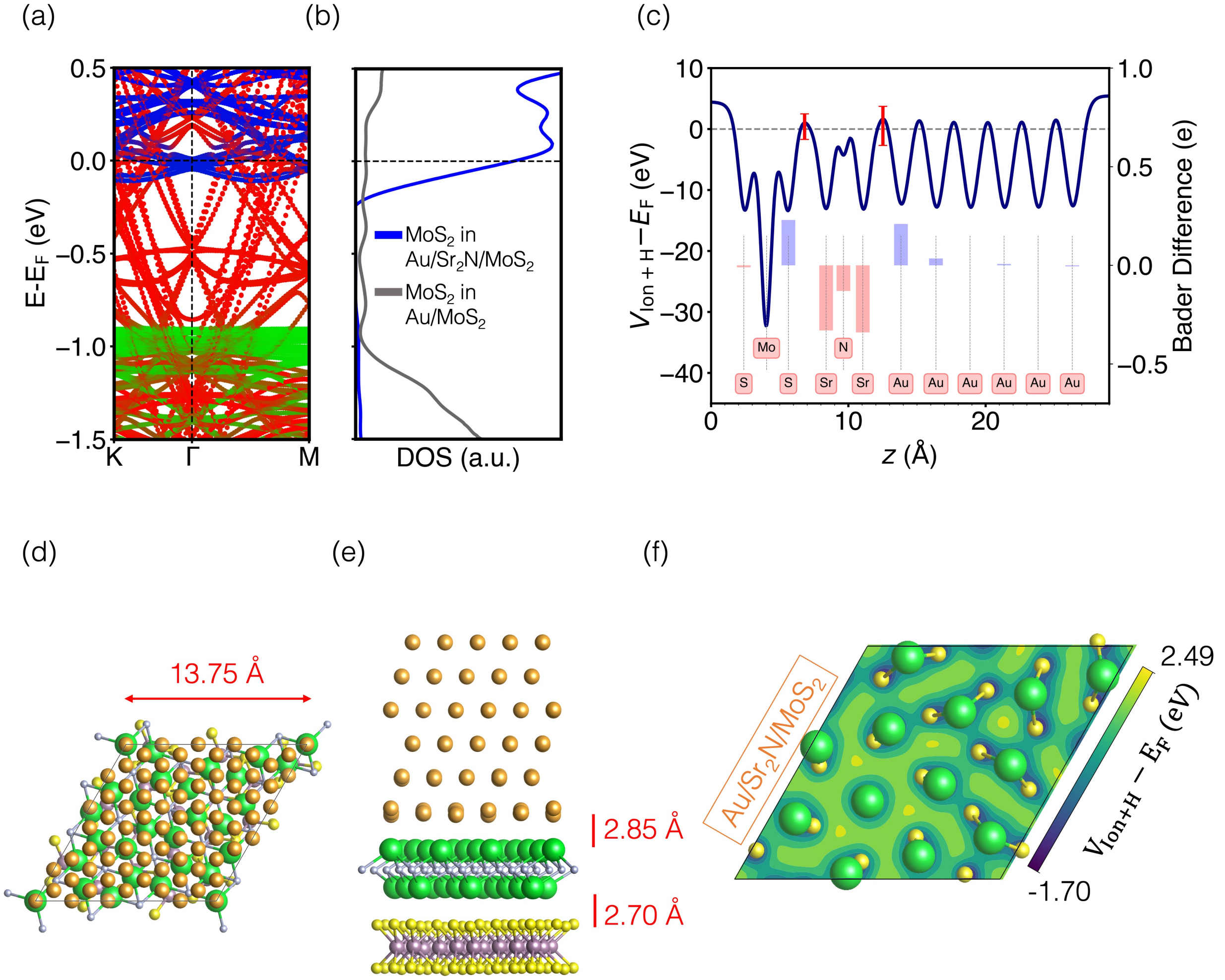

Fig. S 5: Properties of the Au/Sr_2N/MoS_2 heterojunction: (a) materials-projected electronic band structure, (b) densities of MoS_2 states per formula unit, (c) averaged electrostatic potential profile, (d) and (e) top and side views of the interface, and (f) 2D projection of the electrostatic potential at the highest potential point of the electrene/MoS_2 interface.

3.7.3 Au/Sr$_2$P/MoS$_2$

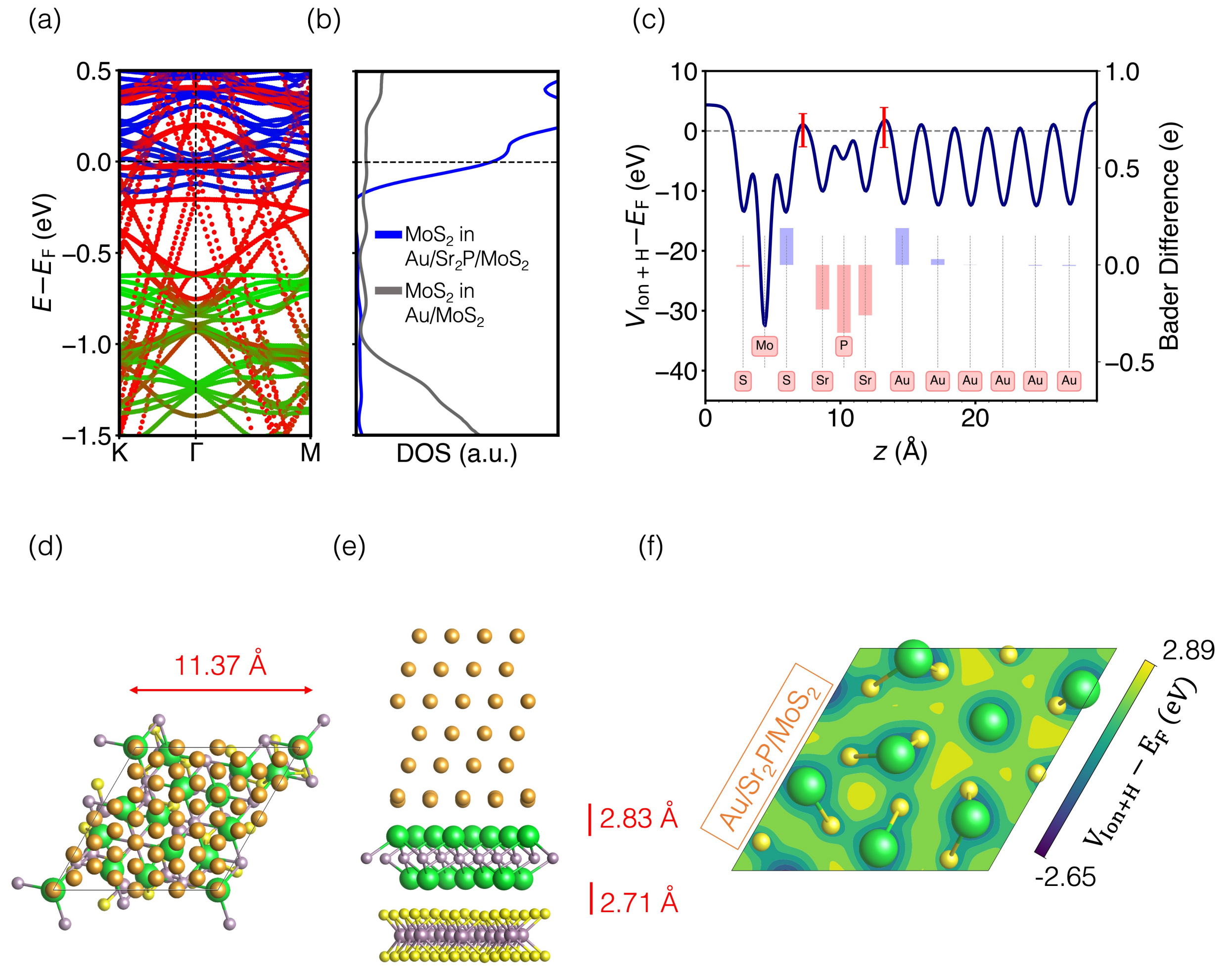

Fig. S 6: Properties of the Au/Sr$_2$P/MoS$_2$ heterojunction: (a) materials-projected electronic band structure, (b) densities of MoS$_2$ states per formula unit, (c) averaged electrostatic potential profile, (d) and (e) top and side views of the interface, and (f) 2D projection of the electrostatic potential at the highest potential point of the electrene/MoS$_2$ interface.

3.7.4 $Au/Ba_2N/MoS_2$

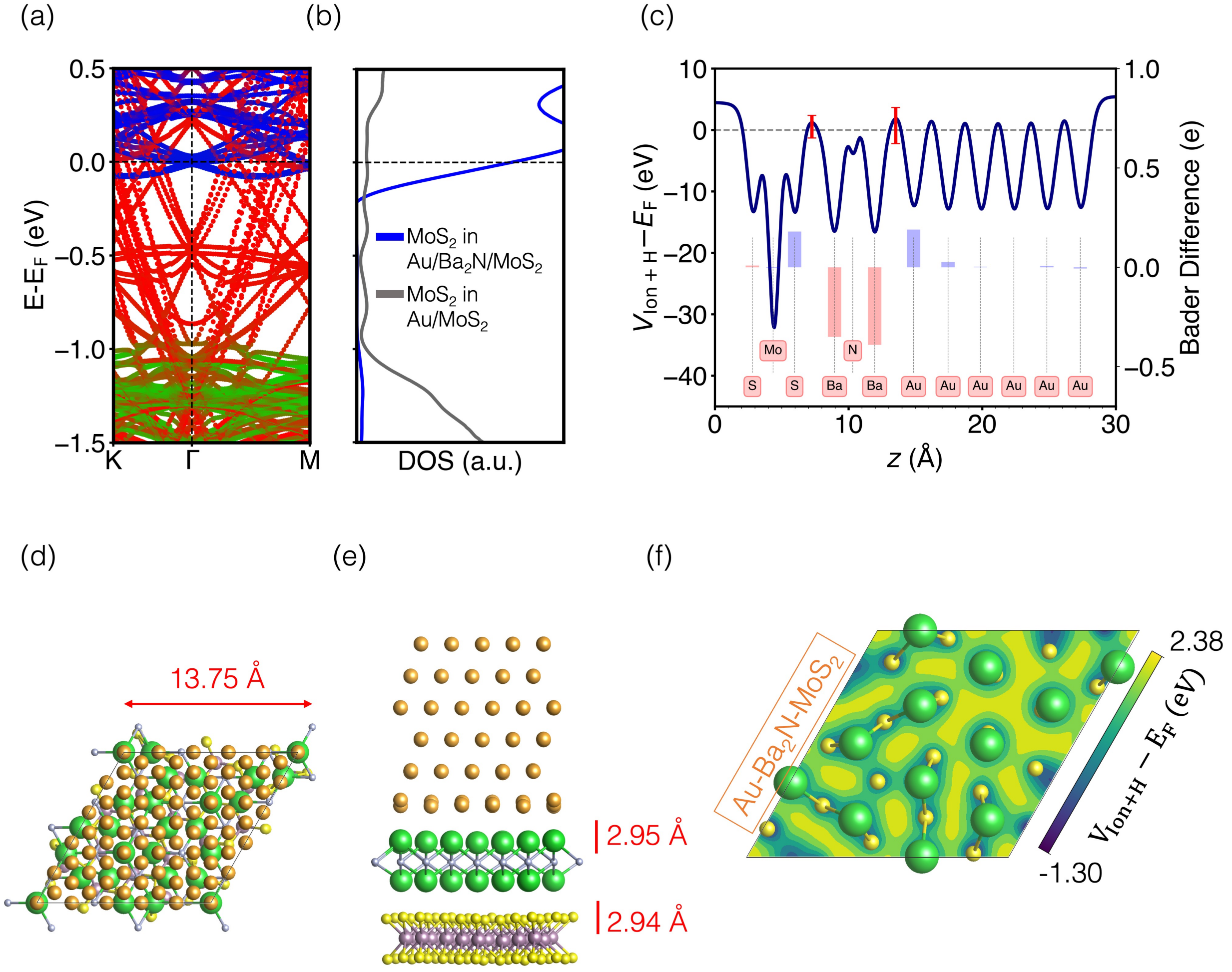

Fig. S7: Properties of the $Au/Ba_2N/MoS_2$ heterojunction: (a) materials-projected electronic band structure, (b) densities of MoS_2 states per formula unit, (c) averaged electrostatic potential profile, (d) and (e) top and side views of the interface, and (f) 2D projection of the electrostatic potential at the highest potential point of the electrene/MoS_2 interface.

3.7.5 $Au/Ba_2P/MoS_2$

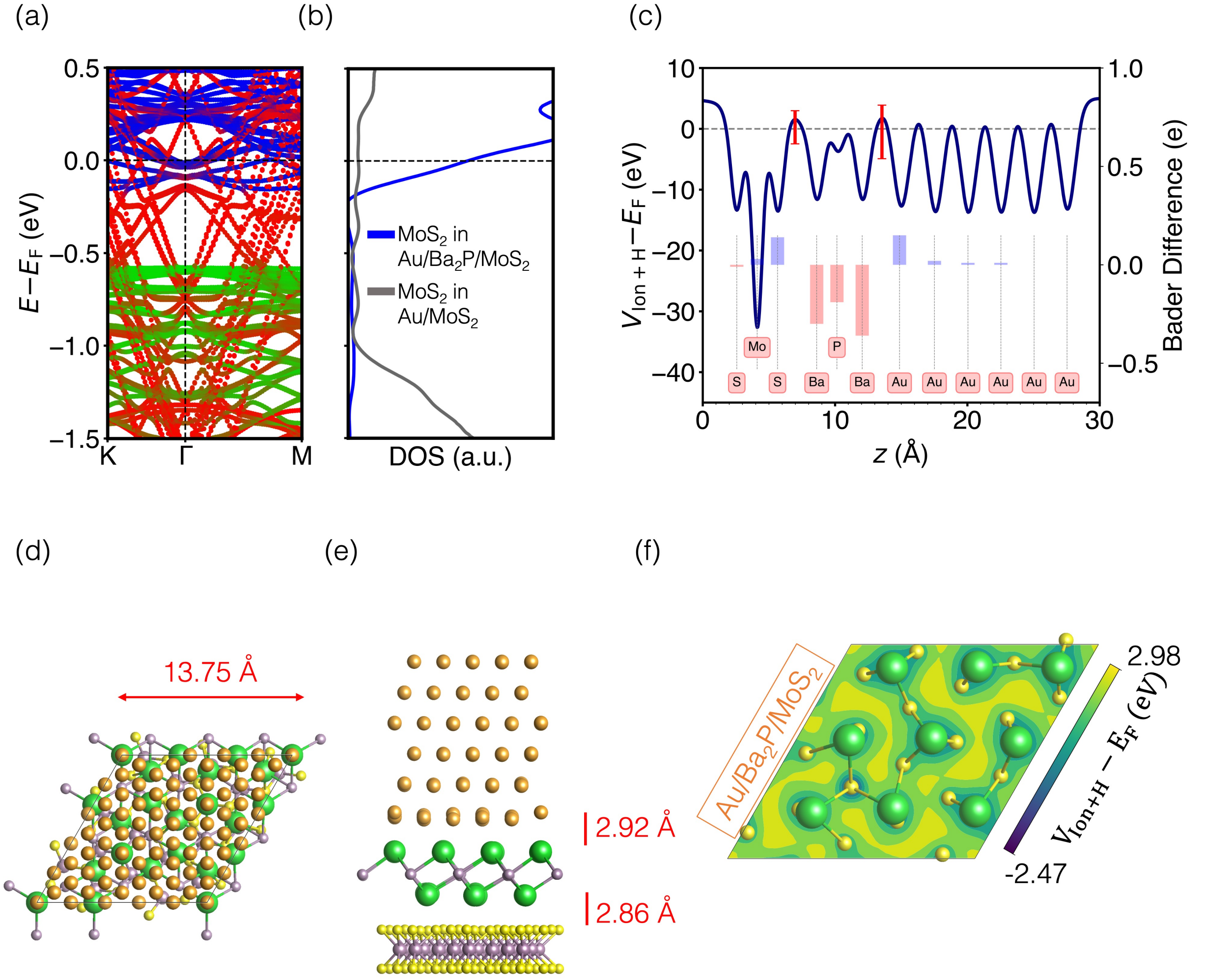

Fig. S8: Properties of the $Au/Ba_2P/MoS_2$ heterojunction: (a) materials-projected electronic band structure, (b) densities of MoS_2 states per formula unit, (c) averaged electrostatic potential profile, (d) and (e) top and side views of the interface, and (f) 2D projection of the electrostatic potential at the highest potential point of the electrene/MoS_2 interface.

3.7.6 Au/Ba_2As/MoS_2

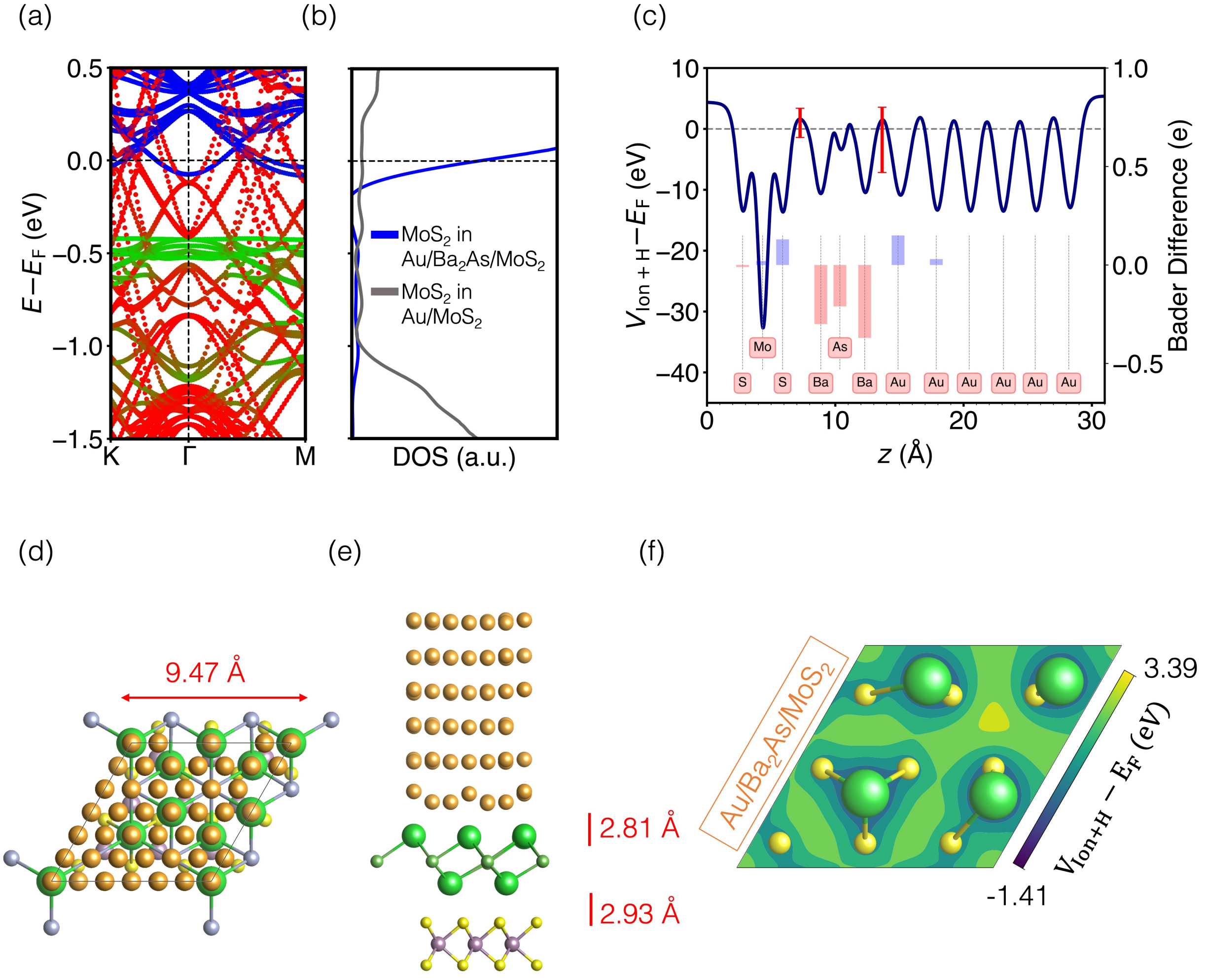

Fig. S 9: Properties of the Au/Ba_2As/MoS_2 heterojunction: (a) materials-projected electronic band structure, (b) densities of MoS_2 states per formula unit, (c) averaged electrostatic potential profile, (d) and (e) top and side views of the interface, and (f) 2D projection of the electrostatic potential at the highest potential point of the electrene/MoS_2 interface.

3.7.7 Au/Ba_2Sb/MoS_2

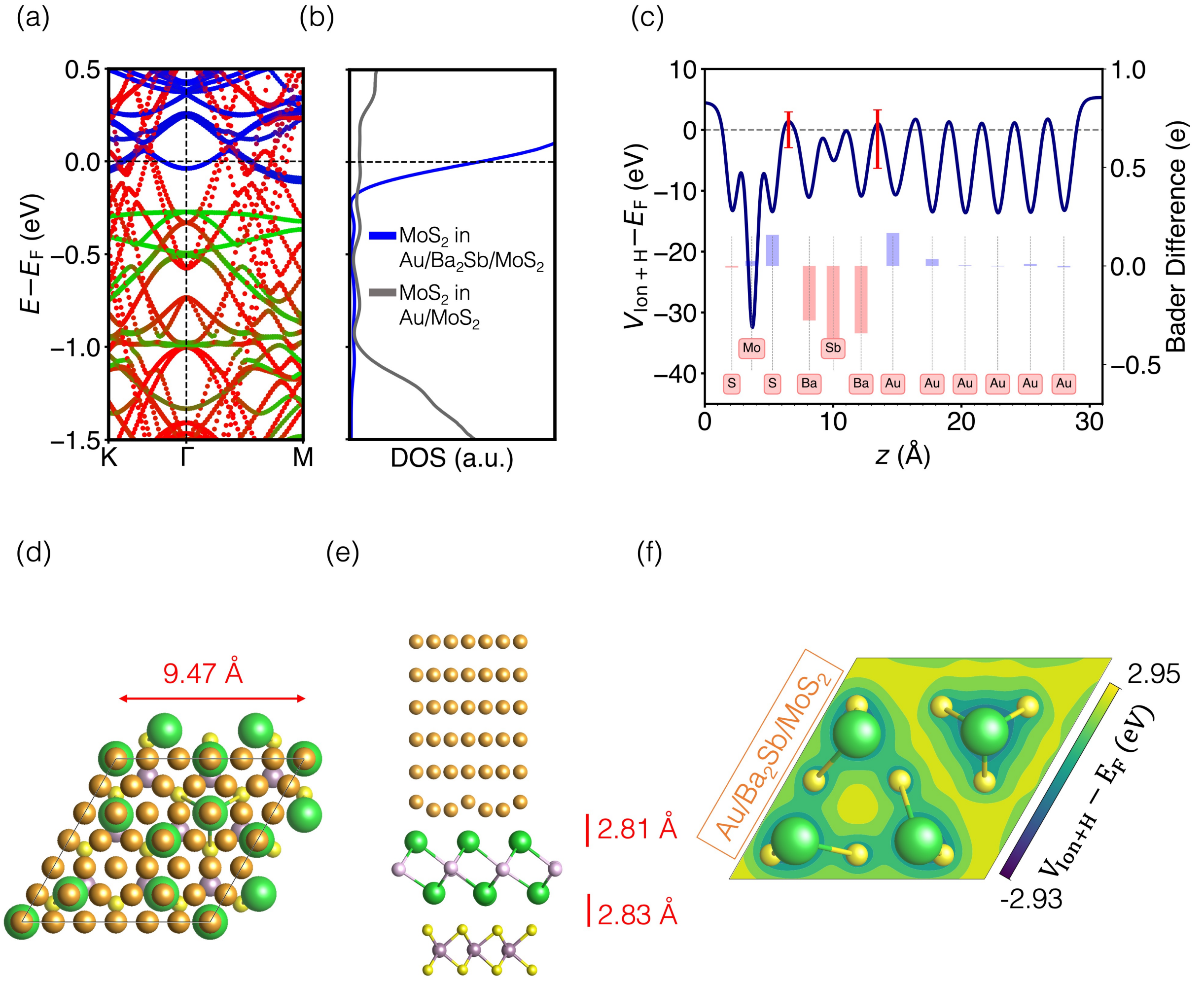

Fig. S 10: Properties of the Au/Ba_2Sb/MoS_2 heterojunction: (a) materials-projected electronic band structure, (b) densities of MoS_2 states per formula unit, (c) averaged electrostatic potential profile, (d) and (e) top and side views of the interface, and (f) 2D projection of the electrostatic potential at the highest potential point of the electrene/MoS_2 interface.

3.8 Electronic Properties of Cu/electrene/MoS_2 Contacts

3.8.1 Cu/Ca_2N/MoS_2

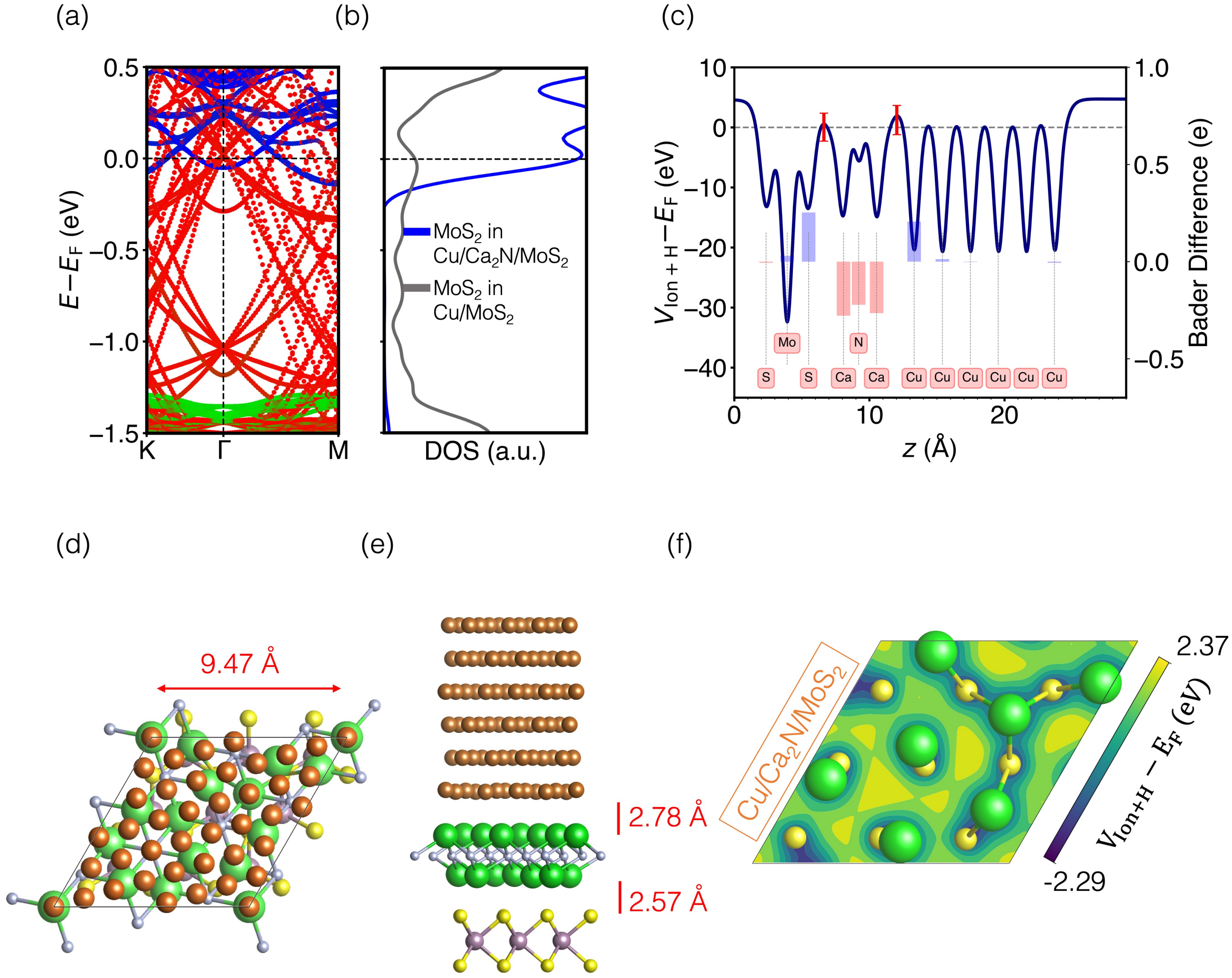

Fig. S 11: Properties of the Cu/Ca_2N/MoS_2 heterojunction: (a) materials-projected electronic band structure, (b) densities of MoS_2 states per formula unit, (c) averaged electrostatic potential profile, (d) and (e) top and side views of the interface, and (f) 2D projection of the electrostatic potential at the highest potential point of the electrene/MoS_2 interface.

3.8.2 $Cu/Sr_2N/MoS_2$

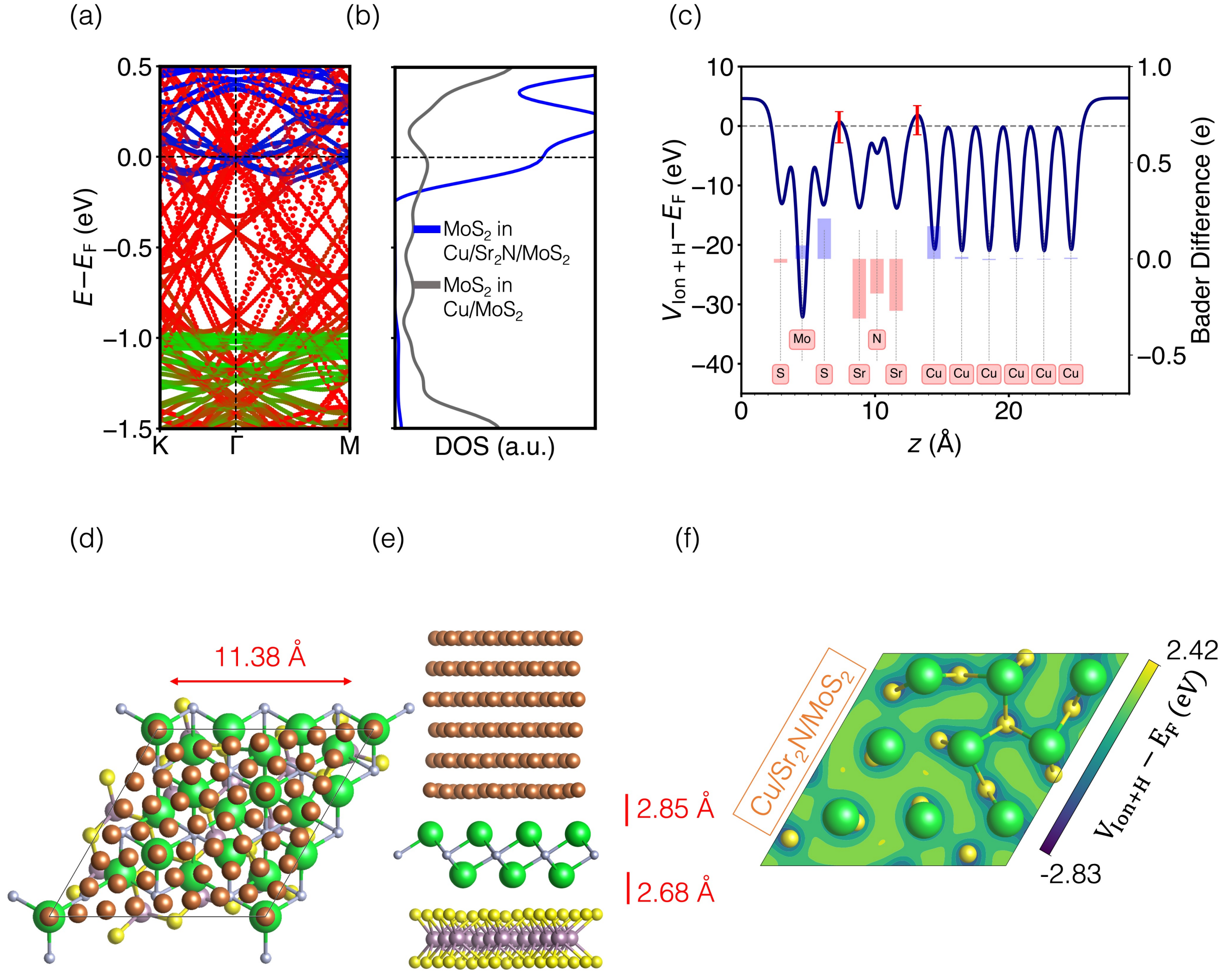

Fig. S12: Properties of the $Cu/Sr_2N/MoS_2$ heterojunction: (a) materials-projected electronic band structure, (b) densities of MoS_2 states per formula unit, (c) averaged electrostatic potential profile, (d) and (e) top and side views of the interface, and (f) 2D projection of the electrostatic potential at the highest potential point of the electrene/MoS_2 interface.

3.8.3 $Cu/Sr_2P/MoS_2$

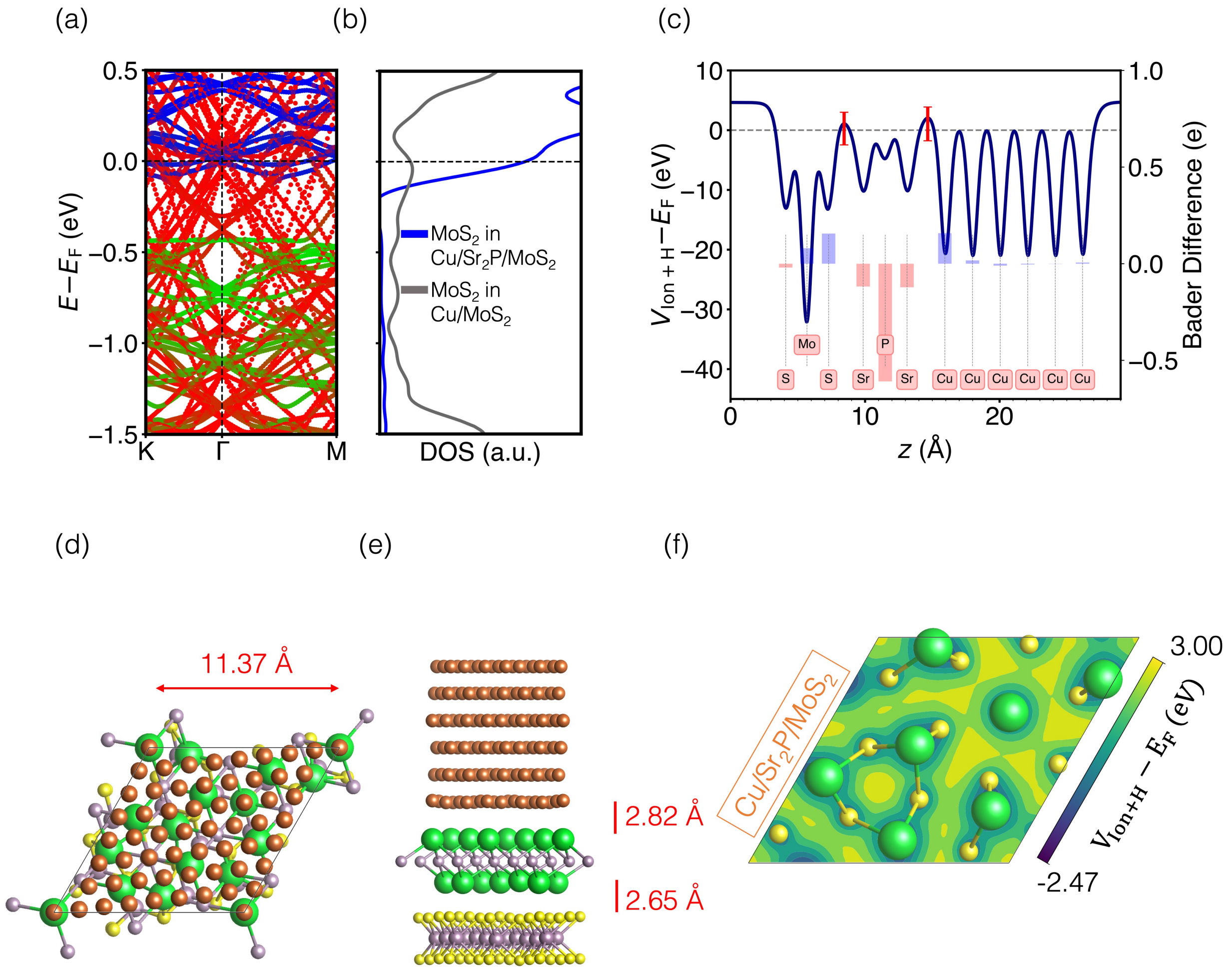

Fig. S13: Properties of the $Cu/Sr_2P/MoS_2$ heterojunction: (a) materials-projected electronic band structure, (b) densities of MoS_2 states per formula unit, (c) averaged electrostatic potential profile, (d) and (e) top and side views of the interface, and (f) 2D projection of the electrostatic potential at the highest potential point of the electrene/MoS_2 interface.

3.8.4 $Cu/Ba_2N/MoS_2$

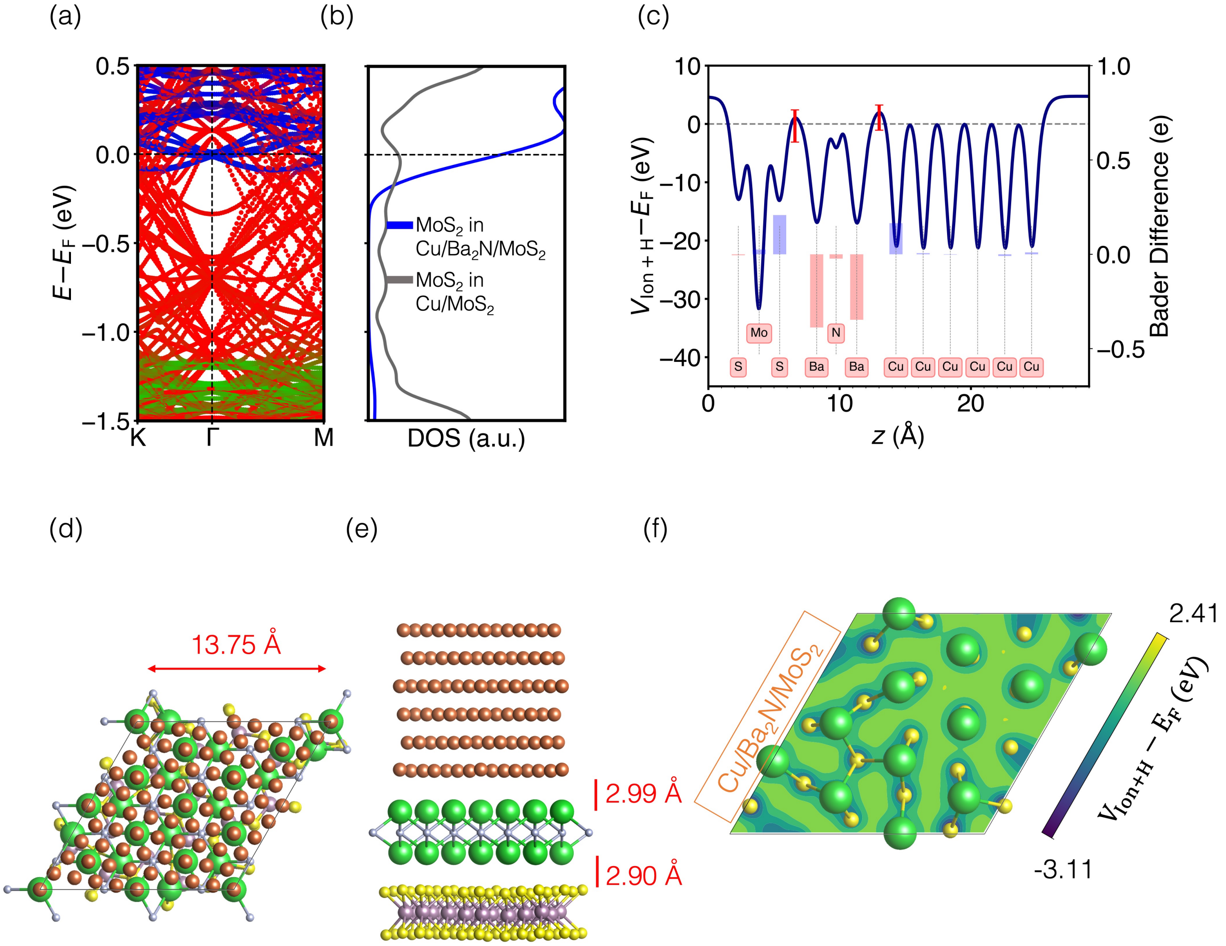

Fig. S 14: Properties of the $Cu/Ba_2N/MoS_2$ heterojunction: (a) materials-projected electronic band structure, (b) densities of MoS_2 states per formula unit, (c) averaged electrostatic potential profile, (d) and (e) top and side views of the interface, and (f) 2D projection of the electrostatic potential at the highest potential point of the electrene/MoS_2 interface.

3.8.5 Cu/Ba_2P/MoS_2

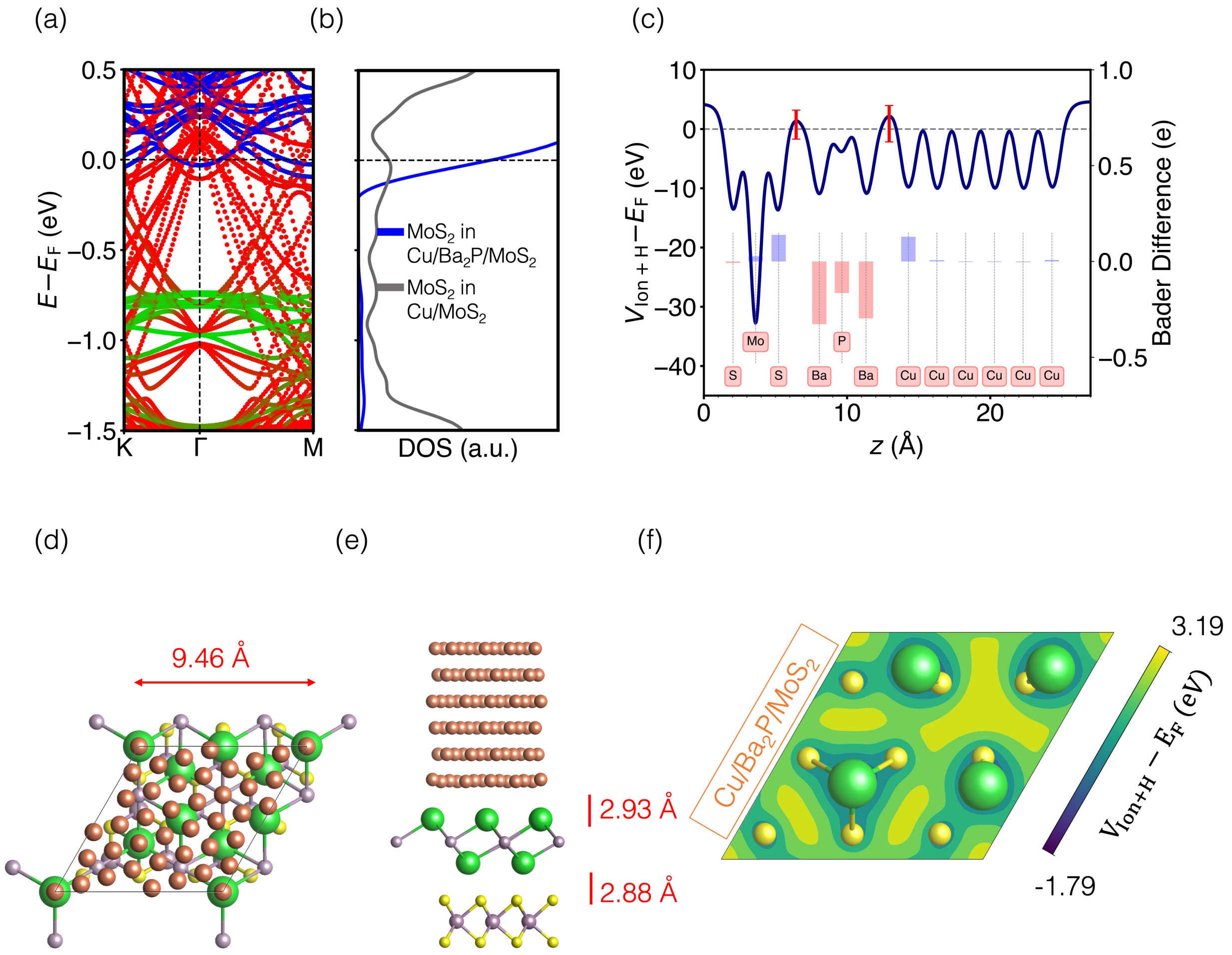

Fig. S 15: Properties of the Cu/Ba_2P/MoS_2 heterojunction: (a) materials-projected electronic band structure, (b) densities of MoS_2 states per formula unit, (c) averaged electrostatic potential profile, (d) and (e) top and side views of the interface, and (f) 2D projection of the electrostatic potential at the highest potential point of the electrene/MoS_2 interface.

3.8.6 $Cu/Ba_2As/MoS_2$

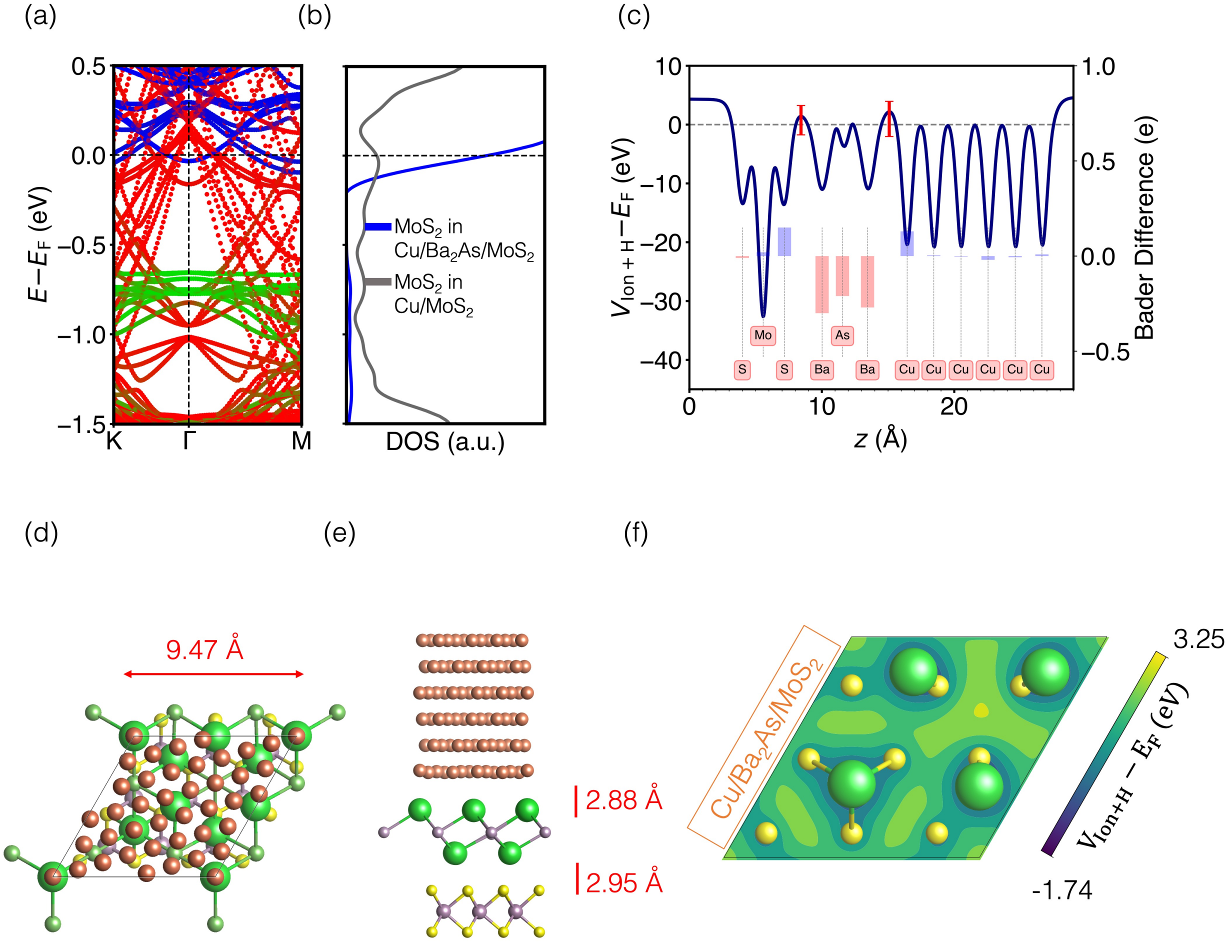

Fig. S 16: Properties of the $Cu/Ba_2As/MoS_2$ heterojunction: (a) materials-projected electronic band structure, (b) densities of MoS_2 states per formula unit, (c) averaged electrostatic potential profile, (d) and (e) top and side views of the interface, and (f) 2D projection of the electrostatic potential at the highest potential point of the electrene/MoS_2 interface.

3.8.7 Cu/Ba_2Sb/MoS_2

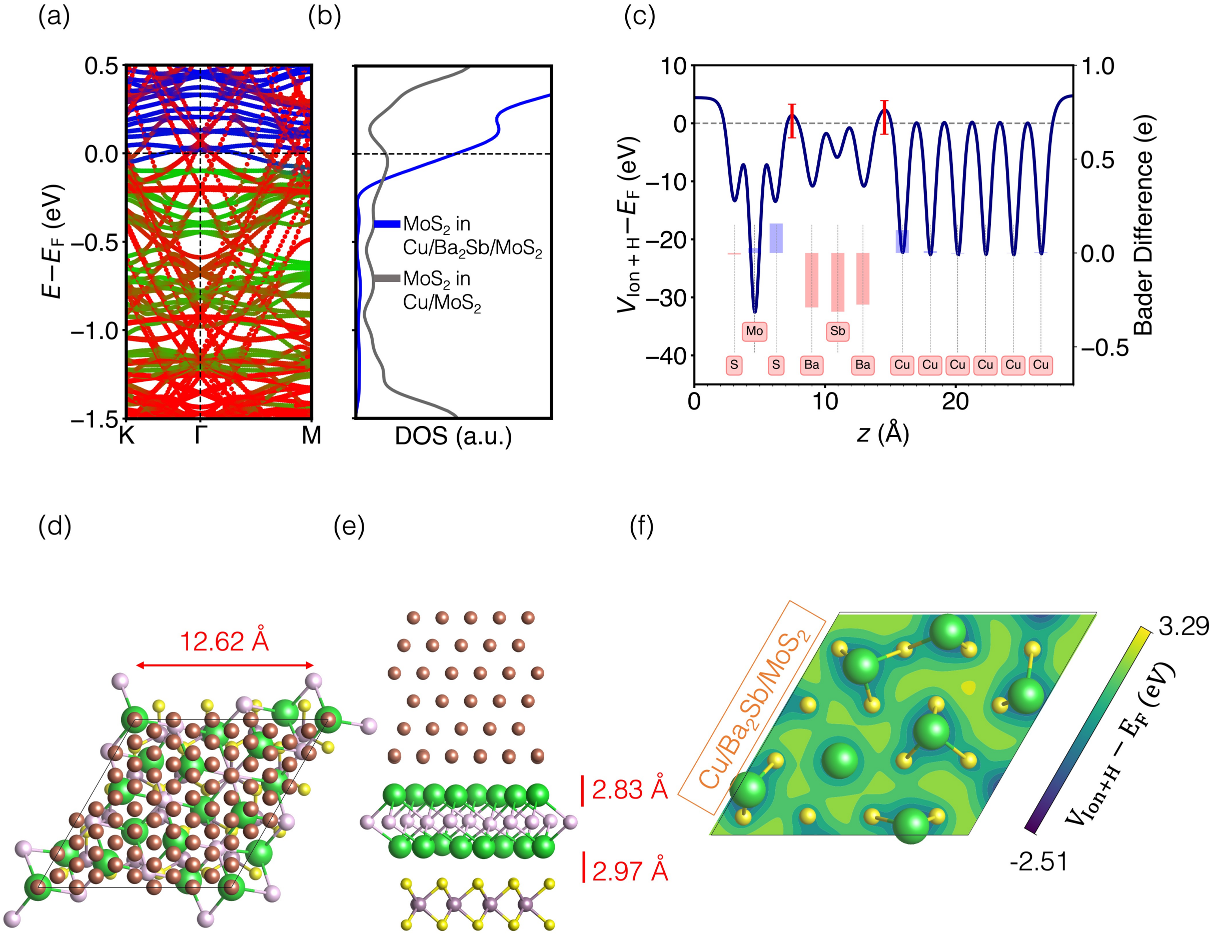

Fig. S 17: Properties of the Cu/Ba_2Sb/MoS_2 heterojunction: (a) materials-projected electronic band structure, (b) densities of MoS_2 states per formula unit, (c) averaged electrostatic potential profile, (d) and (e) top and side views of the interface, and (f) 2D projection of the electrostatic potential at the highest potential point of the electrene/MoS_2 interface.

3.9 Electronic Structure of Isolated Individual Layers

3.9.1 Band Structures of Distorted Layers from Au/Electrene/MoS_2 Interfaces

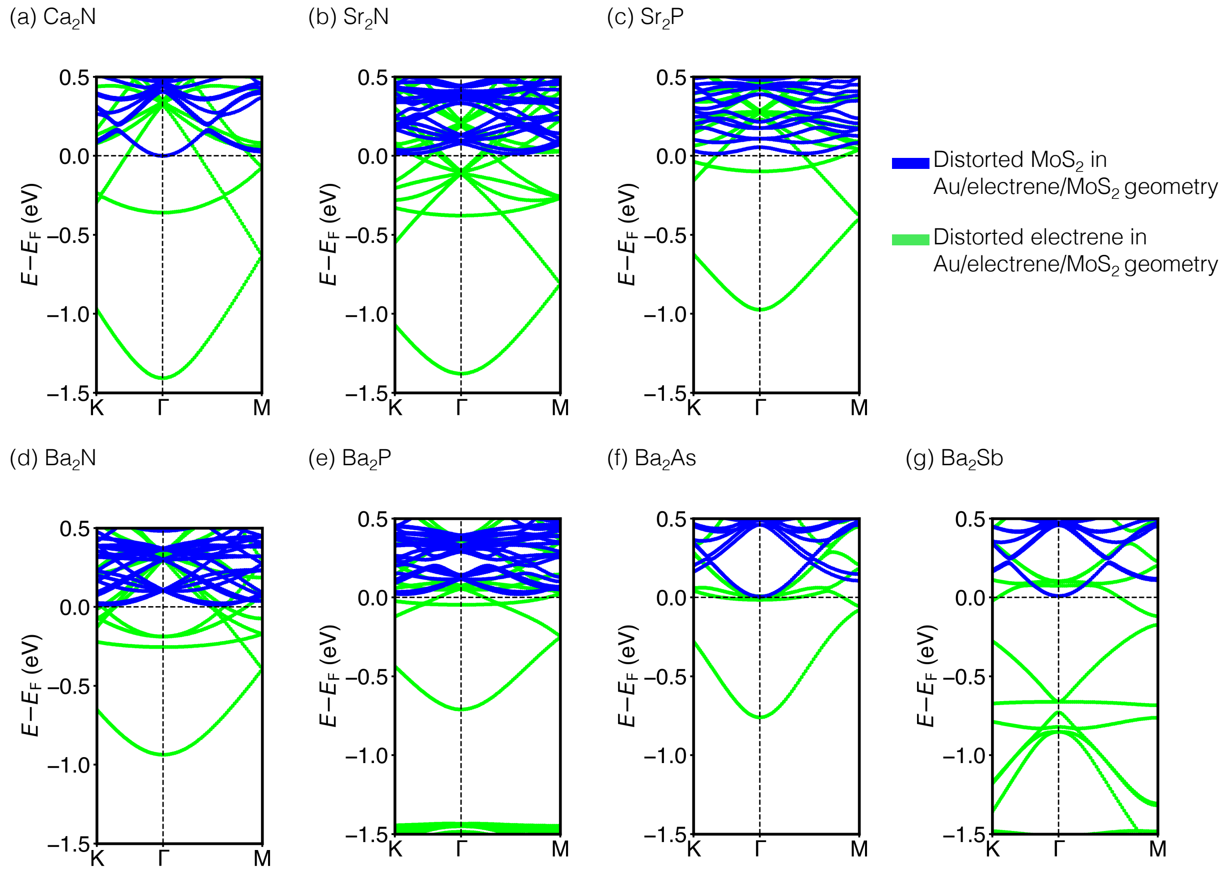

Fig. S 18: Band structures of isolated Ca_2N and MoS_2 layers at rigid, distorted geometries taken from the Au/electrene/MoS_2 interfaces.

3.9.2 Band Structures of Relaxed Layers from Au/Electrene/MoS$_2$ Interfaces

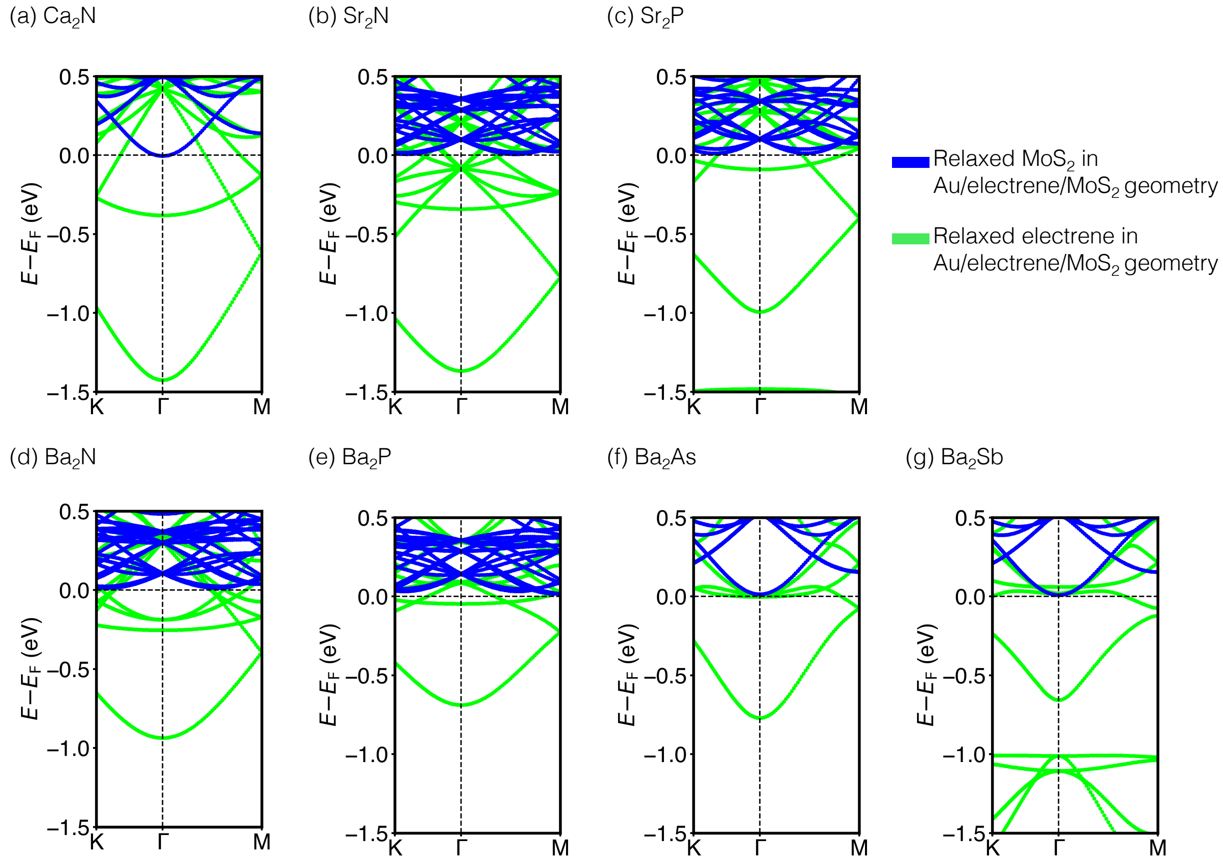

Fig. S19: Band structures of isolated Ca$_2$N and MoS$_2$ layers at relaxed geometries with fixed latticed constants matching those of the Au/electrene/MoS$_2$ interfaces.

3.9.3 Band Structures of Distorted Layers from Cu/Electrene/MoS_2 Interfaces

(a) Ca_2N (b) Sr_2N (c) Sr_2P

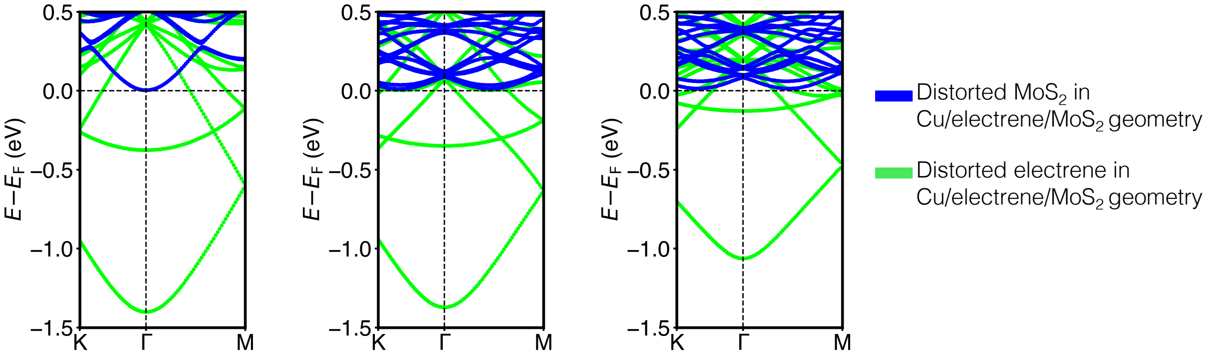

(d) Ba_2N (e) Ba_2P (f) Ba_2As (g) Ba_2Sb

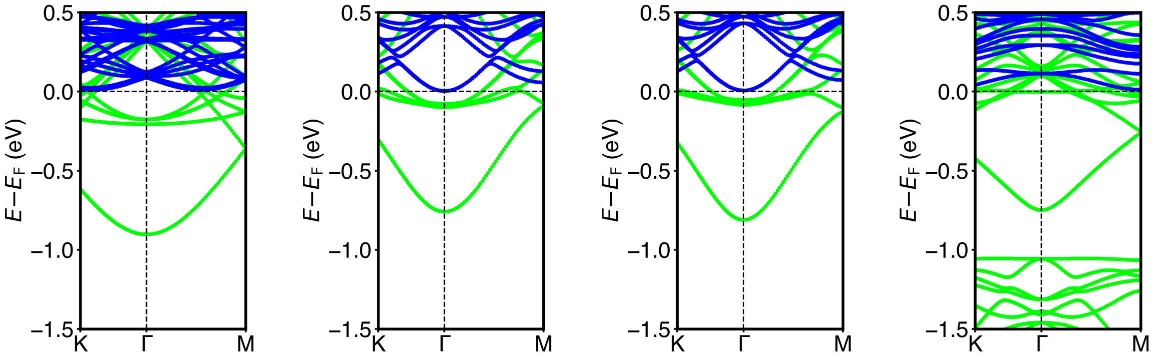

Fig. S 20: Band structures of isolated Ca_2N and MoS_2 layers at rigid, distorted geometries taken from the Cu/electrene/MoS_2 interfaces.

3.9.4 Band Structures of Relaxed Layers from Cu/Electrene/MoS$_2$ Interfaces

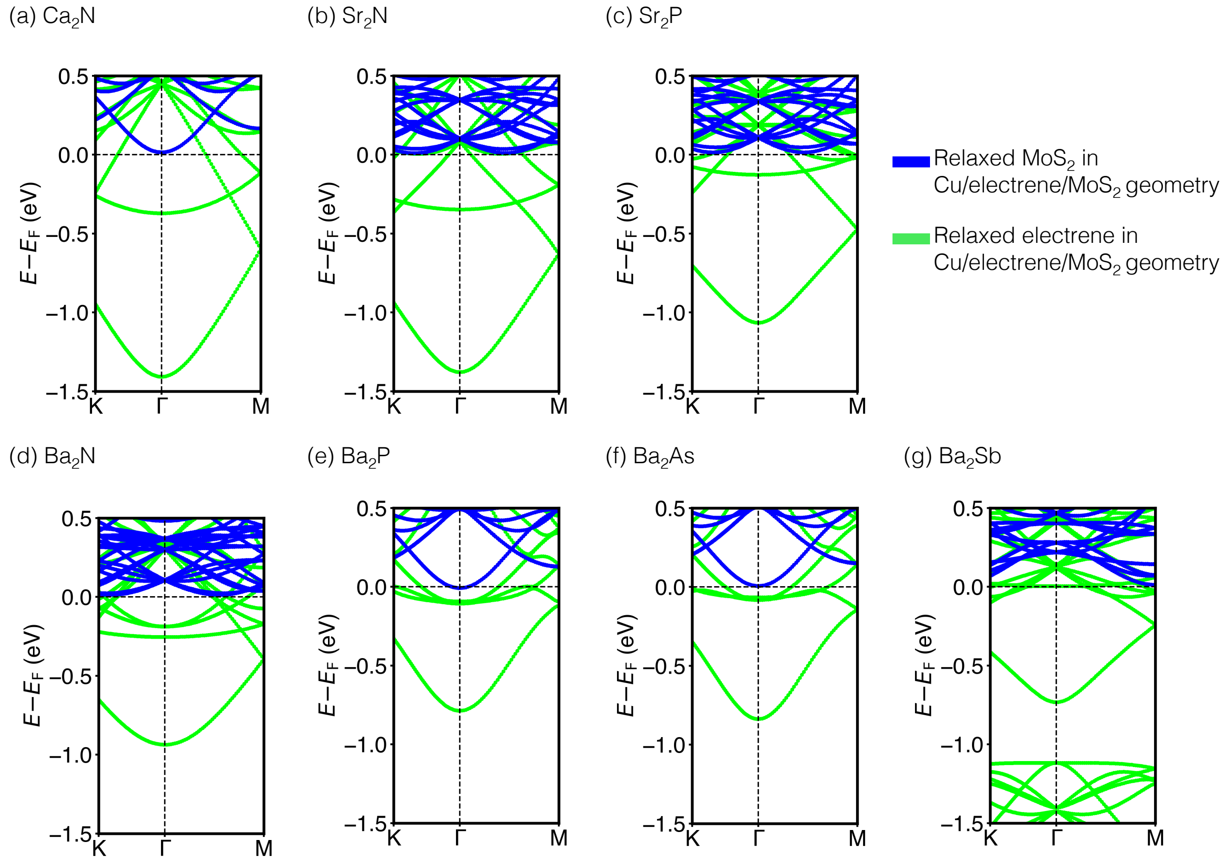

Fig. S21: Band structures of isolated Ca$_2$N and MoS$_2$ layers at relaxed geometries with fixed latticed constants matching those of the Cu/electrene/MoS$_2$ interfaces.

4 Tunnelling Characteristics from the WKB Approximation

Here we discuss the tunnelling probability and tunnelling-specific resistivity based on the WKB approximation.[11,12] Note that the WKB approximation is heavily reliant on the shape of the potential barrier. In its general form in one dimension, the transmission probability, $\mathcal{T}_{\mathrm{WKB}}$, can be written in terms of the relative amplitudes of the transmitted (F) and incident (A) waves,

$$\mathcal{T}_{\mathrm{WKB}} = \frac{|F|^2}{|A|^2} \approx e^{-2\gamma},$$

which can be approximated in terms of the γ parameter obtained by integrating the area under the potential curve, $V(x)$:

$$\gamma = \frac{\sqrt{2m}}{\hbar} \int_{x_1}^{x_2} \sqrt{V(x) - E}\, dx,$$

where $x_{1,2}$ are the classical turning points at which $E = V(x_{1,2})$.

Assuming a square-shaped barrier, the tunnelling probability can be evaluated in terms of the tunneling barrier height (TBH) and tunneling barrier width (TBW) as

$$\mathcal{T}_{\mathrm{WKB}} = \exp\left(-\frac{4\pi}{h}\mathrm{TBW}\sqrt{2m_{\mathrm{e}}\mathrm{TBH}}\right),$$

while the tunneling resistivity, ρ_t, is

$$\rho_t = \frac{2h^2\mathrm{TBW}}{3e^2\sqrt{2m_{\mathrm{e}}\ \mathrm{TBH}}} \exp\left(\frac{4\pi}{h}\mathrm{TBW}\sqrt{2m_e\mathrm{TBH}}\right).$$

The computed values of $\mathcal{T}_{\mathrm{WKB}}$ and ρ_t for the various metal/electrene/MoS$_2$ heterojunctions are shown in Figure S22.

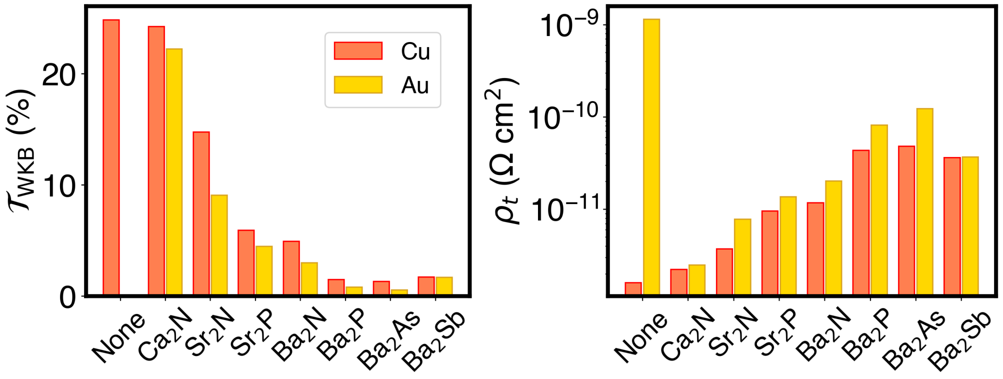

Fig. S22: The WKB tunnelling probability ($\mathcal{T}_{\mathrm{WKB}}$, left) and the tunnelling specific resistivity (ρ_t, right) of the metal/electrene/MoS_2 interfaces, calculated by assuming a square potential.

References

(1) Gong, C.; Colombo, L.; Wallace, R. M.; Cho, K. The Unusual Mechanism of Partial Fermi Level Pinning at Metal–MoS_2 Interfaces. *Nano Lett.* **2014**, *14*, 1714–1720.

(2) Farmanbar, M.; Brocks, G. Controlling the Schottky Barrier at MoS_2/Metal Contacts by Inserting a BN Monolayer. *Phys. Rev. B* **2015**, *91*, 161304.

(3) Helfrecht, B. A.; Guzman, D. M.; Onofrio, N.; Strachan, A. H. Interactions Between Copper and Transition Metal Dichalcogenides: A Density Functional Theory Study. *Phys. Rev. Mater.* **2017**, *1*, 034001.

(4) Allain, A.; Kang, J.; Banerjee, K.; Kis, A. Electrical Contacts to Two-Dimensional Semiconductors. *Nat. Mater.* **2015**, *14*, 1195–1205.

(5) Liu, W.; Kang, J.; Cao, W.; Sarkar, D.; Khatami, Y.; Jena, D.; Banerjee, K. High-Performance Few-Layer MoS_2 Field-Effect-Transistor with Record Low Contact-Resistance. 2013 IEEE Intl. Electron Device Mtg. 2013; pp 19–4.

(6) Kang, J.; Liu, W.; Sarkar, D.; Jena, D.; Banerjee, K. Computational Study of Metal Contacts to Monolayer Transition-Metal Dichalcogenide Semiconductors. *Phys. Rev. X* **2014**, *4*, 031005.

(7) Kaadou, F.; Maassen, J.; Johnson, E. R. Improved Charge Transfer and Barrier Lowering across a Au–MoS_2 Interface through Insertion of a Layered Ca_2N Electride. *J. Phys. Chem. C* **2021**, *125*, 11656–11664.

(8) Price, A. J. A.; Otero de la Roza, A.; Johnson, E. R. XDM-corrected hybrid DFT with numerical atomic orbitals predicts molecular crystal lattice energies with unprecedented accuracy. *Chem. Sci.* **2023**, *14*, 1252–1262.

(9) Blum, V.; Gehrke, R.; Hanke, F.; Havu, P.; Havu, V.; Ren, X.; Reuter, K.; Schef-

fler, M. Ab initio molecular simulations with numeric atom-centered orbitals. *Comp. Phys. Comm.* **2009**, *180*, 2175–2196.

(10) van Lenthe, E.; Baerends, E. J.; Snijders, J. G. Relativistic total energy using regular approximations. *J. Chem. Phys.* **1994**, *101*, 9783–9792.

(11) Griffiths, D. J.; Schroeter, D. F. *Introduction to Quantum Mechanics*; Cambridge university press, 2018.

(12) Simmons, J. G. Generalized Formula for the Electric Tunnel Effect Between Similar Electrodes Separated by a Thin Insulating Film. *J. Appl. Phys.* **1963**, *34*, 1793–1803.